Microwave Scattering from Dielectric Wedges with Planar Surfaces: A Diffraction Coefficient Based on a Physical Optics Version of GTD

R. E. Burge, X.-C. Yuan, B. D. Carroll, N. E. Fisher, T. J. Hall, G. A. Lester, N. D. Taket, and Chris J. Oliver

***Abstract*—The development is presented here, derived from a physical optics version of the geometrical theory of diffraction (POGTD) of a simple edge coefficient for external and internal diffraction at planar dielectric edges. This is required in connection with a simulator for synthetic aperture radar (SAR) images. The diffraction coefficient is assessed by comparison of calculations using POGTD, excluding multiple scattering processes, with an extensive set of experimental microwave scattering data on dielectric wedges and some corresponding calculations by the finite-difference time-domain method (FDTD) of solving Maxwell's equations. The experimental results were gained from dielectric wedges of four wedge angles, each for a wide range of angles of incidence, separately for TE and TM plane polarized components, and for two sets of wedges with different dielectric constants. The intensity distribution found by using the diffraction coefficient for external diffraction is found to be in good agreement with both experiment and calculations using FDTD. For internal wedge diffraction, POGTD predicts an intensity distribution of similar angular shape to the experimental but, due to the neglect of absorption, the intensity level is too high.**

***Index Terms*— Dielectric bodies, electromagnetic scattering, wedges.**

I. Introduction

THIS work originated from the need to include edge diffraction in a numerical simulator for the imaging of urban areas by airborne synthetic aperture radar (SAR) [1]. Edge diffraction is important because the main contributions to coherent high-frequency scattering are local phenomena associated with specular points at surfaces and edges [2], [3] or object-to-object interactions within a scene [1]. These two effects are distinguished as the first principally concerned reflected rays and edge-diffracted rays and the second either reflected or transmitted rays and edge-diffracted rays. The simulator separately considers specular and diffuse imaging and is intended to provide semi-quantitative estimations of the expected SAR images from urban models. The present work, which is self-contained, accounts for microwave diffraction at planar dielectric edges by a version of the geometrical theory of diffraction (GTD) [4] based on physical optics (PO) and compares calculated and experimental results under laboratory conditions. The field distribution of scattered microwave radiation for a dielectric wedge is given by the superposition, accounting for phase relationships of the geometrical optics field and the fields due to diffraction, both externally and internally, at the edge of the wedge. We address here the description of the external and internal wedge-diffraction coefficient. As compared with a wedge of perfectly conducting material, account must be taken of fields transmitted into the wedge material and transmitted or internally reflected at the emergent face.

Our initial formulation of diffraction coefficients for wedges and vertices with planar surfaces by POGTD [5] was limited in its application to perfectly conducting objects. The level of agreement [5], [6] in initial tests of POGTD for edges and corners of metal plates was very satisfactory. Of course, this approach to the wedge diffraction coefficients follows on from a very extensive literature of the developments of the original form of GTD for a perfectly conducting wedge (e.g., the uniform theory of diffraction (UTD) [7] and the uniform asymptotic theory of diffraction (UAT) [8] recently continued, for example, [9], [10]) to overcome, in a wide range of applications, limitations associated with incident and reflected shadow boundaries.

Scattering models are required for the simulator that are sufficiently valid in general trends not to be misleading, but are not necessarily fully quantitative when used to assist the interpretation of real SAR images. Real buildings do not have sharp edges and flat surfaces such as those used in calculations and flexibility is a requirement for image interpretation. A similar view, comparing the results of a limited theoretical treatment with experimental data, has been taken [11] when using a UTD calculation based on multiple wedge diffractions to predict the propagation of high-frequency electromagnetic waves over basically random hilly terrain where edges do not tend to lie on straight lines.

Rubin [12] has reviewed the rather small number of complete approaches to the general problem of assemblies of

Manuscript received August 27, 1998; revised July 23, 1999. This work was supported by DERA, Malvern. The work of R. E. Burge was supported by the Leverhulme Trust.

R. E. Burge is with the Physics Department, University of London King's College, Strand, London, WC2R 2LS U.K.

X.-C. Yuan, B. D. Carroll, N. E. Fisher, T. J. Hall, G. A. Lester, and N. D. Taket are with the Physics Department, University of London King's College, Strand, London, WC2R 2LS U.K.

C. J. Oliver is with Defence Evaluation and Research Agency, Malvern, WR14 3PS U.K.

Publisher Item Identifier S 0018-926X(99)09382-5.

fully-defined conducting and dielectric objects, e.g., moment methods [13]–[15], surface equivalence principles [16], [17], and we may add, selected from a range of commercially available software, the finite-element and finite-difference time-domain (FDTD) techniques, e.g., [18], [19], which allow the calculation of internal and external fields for conductors and dielectrics. With the rapid contemporary advances in computing power, there is much current interest [19] in the FDTD method, but the computation involved for more than simple objects is still formidable. In GTD, for a detailed object model, identified multiple as well as single scattering interactions can be separately included, while FDTD involves all the possible interactions of whatever scattering order.

We are interested in identifying the diffraction coefficient for external and internal diffraction at a dielectric edge without confusion due to the effects of object-specific "multiple bounce" transmission or reflection at the material surfaces. In the experiments conducted with dielectric wedges the wedge angles are such that the effects of such multiple interactions occur at scattering angles far from the shadow region where the diffraction coefficient operates. Accordingly, our analysis of POGTD assumes singly reflected and singly transmitted ray components, that each face of the wedge can be treated separately, and that the faces only interact through their geometrical optics fields. Absorption is neglected or its effects must be introduced empirically to the internal diffraction coefficient; this provides a limitation to the application of the method. Other possible optical processes arising from the interactions of the reflected and transmitted rays, e.g., surface waves and surface wave diffraction, are considered in terms of the differences between theoretical and experimental intensity distributions.

As background to considering multiple scattering in a transmitting dielectric wedge, the effects for conducting materials of multiple reflections, multiple diffractions, and reflection-diffractions and reflected-diffracted reflections as associated with, for example, edge diffraction from rectangular flat plates, dihedral corner reflectors, and appendages on a smooth surface have been considered (e.g., [20]–[22]). The impedance boundary condition, which includes material effects but avoids the calculation of fields within the material, has been used to formulate the electromagnetic fields scattered by both interior and exterior impedance wedges [23], [24] and, for example, to evaluate scattering at edges of surface impedance discontinuities on a flat ground plane [25]. The calculations, made in [24] for the interior wedge, account for multiple reflected fields of any order within the wedge to produce a diffraction coefficient of UTD form for a wedge of arbitrary angle. Particularly relevant to our work on dielectric wedges is the work of Burnside and Burgener [26] who consider modifications to UTD to deal with the high-frequency scattering in transmission and reflection, including multiple internal reflections by a thin parallel-sided dielectric slab.

The experimental work described here is for wedges with permittivities, measured for us by GEC-Marconi plc, Towcester, U.K., of either 1.86 or 3.1 for 1-cm microwaves. The loss tangents in both cases were $\sim 10^{-2}$. Representative calculations of the distribution of scattered microwave intensity were carried out by the FDTD method, including absorption and are used to consider the effects of multiple scattering interactions excluded from POGTD on the distribution of scattered intensity. The FDTD calculations also enable corrections for small experimental misalignments of the wedges. A small anechoic chamber was constructed for these measurements.

II. Extension of POGTD to Scattering by Dielectric Materials

Essentially, as in [5] but now for a homogeneous dielectric, the Helmholtz–Kirchoff expression [27] over a surface is evaluated to give the total scattered field as the integral of the total surface field, where the latter in PO is represented by the geometrical optics field and assumes that the surface is smooth and fully illuminated by the incident wave. The asymptotic integration is carried out by the method of stationary phase [28] according to which the principal contributions to the surface integral arise from the neighborhood of three critical points. Critical points of the second kind correspond to the edge-diffraction points and the scattered fields from these points give the edge-diffracted field.

We consider a dielectric wedge defined as very wide and very long and symmetrically orientated in respect to the incident microwaves, i.e., the microwaves may be regarded as incident in the plane of the paper while the wedge surfaces are in planes perpendicular to that plane; the scattering problem is thus two-dimensional (2-D). Generalizations of GTD to include obliquely incident rays [29] have been considered.

We restrict the details of the analysis (see [5]) to those necessary to generalize it from the conducting to the dielectric case. The incident field is assumed to be a geometrical optics field incident on the surface of the scattering object at $\boldsymbol{r_0}$; the direction of this ray is denoted by $\hat{\boldsymbol{k}}_{\boldsymbol{i}}$. At $\boldsymbol{r_0}$ the incident wavefront is assumed to have principal radii of curvature ρ_1 and ρ_2 and the two orthonormal vectors $\hat{\boldsymbol{x}}_{\boldsymbol{1}}$ and $\hat{\boldsymbol{x}}_{\boldsymbol{2}}$ in combination with $\hat{\boldsymbol{k}}_{\boldsymbol{i}}$, to which they are orthogonal, define the principal planes of curvature. The incident field as in synthetic aperture radar imaging is assumed to be diverging at $\boldsymbol{r_0}$, so that ρ_1 and ρ_2 are both positive. Thus, at a distance R from $\boldsymbol{r_0}$ along this ray the incident field is given by

$$\boldsymbol{E_i}(\boldsymbol{r_0}+R\hat{\boldsymbol{k}}_{\boldsymbol{i}}) = \boldsymbol{E_i}(\boldsymbol{r_0})e^{ikR}\sqrt{\frac{\rho_1\rho_2}{(\rho_1+R)(\rho_2+R)}}. \quad (1)$$

An incident ray will, in general, produce reflected and transmitted rays with reflected ray direction given by

$$\hat{\boldsymbol{k}}_{\boldsymbol{r}} = \hat{\boldsymbol{k}}_{\boldsymbol{i}} - 2\hat{\boldsymbol{k}}_{\boldsymbol{i}}\cdot\hat{\boldsymbol{n}}\hat{\boldsymbol{n}} \quad (2)$$

where $\hat{\boldsymbol{n}}$ is the normal to the surface of the scattering object and is defined to point into the interior of the scattering object. The strength of the reflected field can be calculated using the Fresnel relations. We define horizontal and vertical polarization vectors for the incident field as

$$\hat{\boldsymbol{a}}_{\boldsymbol{iH}} = \frac{\hat{\boldsymbol{k}}_{\boldsymbol{i}}\times\hat{\boldsymbol{n}}}{|\hat{\boldsymbol{k}}_{\boldsymbol{i}}\times\hat{\boldsymbol{n}}|}, \quad \hat{\boldsymbol{a}}_{\boldsymbol{iV}} = \hat{\boldsymbol{k}}_{\boldsymbol{i}}\times\hat{\boldsymbol{a}}_{\boldsymbol{iH}} \quad (3)$$

with a vertical polarization vector for the reflected field as

$$\hat{\boldsymbol{a}}_{\boldsymbol{rV}} = \hat{\boldsymbol{k}}_{\boldsymbol{r}}\times\hat{\boldsymbol{a}}_{\boldsymbol{iH}} \quad (4)$$

horizontal and vertical reflection coefficients as

$$R_H = \frac{p_1 - p_2}{p_1 + p_2}, \qquad R_V = \frac{\epsilon p_1 - p_2}{\epsilon p_1 + p_2} \tag{5}$$

where

$$p_1 = \sqrt{1 - |\hat{\boldsymbol{k}}_{\boldsymbol{i}} \times \hat{\boldsymbol{n}}|^2}, \qquad p_2 = \sqrt{\epsilon - |\hat{\boldsymbol{k}}_{\boldsymbol{i}} \times \hat{\boldsymbol{n}}|^2}. \tag{6}$$

For a field propagating from one medium (exterior) to a second medium (interior) the complex permittivity of the interior medium relative to the exterior medium is defined as ϵ. The reflection properties of the surface for this incident field may be described by the reflection dyadic

$$\overline{\boldsymbol{R}} = \hat{\boldsymbol{a}}_{\boldsymbol{iH}} R_H \hat{\boldsymbol{a}}_{\boldsymbol{iH}} + \hat{\boldsymbol{a}}_{\boldsymbol{rV}} R_V \hat{\boldsymbol{a}}_{\boldsymbol{iV}}. \tag{7}$$

The reflected electric field at a distance of R from $\boldsymbol{r_0}$ along the ray reflected from $\boldsymbol{r_0}$ is then

$$\boldsymbol{E_r}\left(\boldsymbol{r_0} + R\hat{\boldsymbol{k}}_{\boldsymbol{r}}\right) = \overline{\boldsymbol{R}} \cdot \boldsymbol{E_i}(\boldsymbol{r_0}) e^{ikR} \sqrt{\frac{\rho_1 \rho_2}{(\rho_1 + R)(\rho_2 + R)}}. \tag{8}$$

The transmitted ray direction at a planar dielectric interface is given by

$$\hat{\boldsymbol{k}}_{\boldsymbol{t}} = \frac{1}{\sqrt{\epsilon}} \left[\hat{\boldsymbol{n}} \sqrt{(\hat{\boldsymbol{n}} \cdot \hat{\boldsymbol{k}}_{\boldsymbol{i}})^2 + \epsilon - 1} + \hat{\boldsymbol{k}}_{\boldsymbol{i}} - \hat{\boldsymbol{n}} \hat{\boldsymbol{n}} \cdot \hat{\boldsymbol{k}}_{\boldsymbol{i}} \right]. \tag{9}$$

For transmitted fields in this formulation ϵ is restricted to real values. If the argument of the square root in this equation is negative then the incident ray is totally internally reflected and there is no transmitted field. The evanescent waves that are in reality produced in such circumstances do not appear in POGTD as it is an asymptotic method. Thus, if there is a transmitted ray, $\hat{\boldsymbol{k}}_{\boldsymbol{t}}$ is a real vector. The strength of the transmitted ray is also given by the Fresnel relations. We define a vertical polarization vector for the transmitted field by

$$\hat{\boldsymbol{a}}_{\boldsymbol{tV}} = \hat{\boldsymbol{k}}_{\boldsymbol{t}} \times \hat{\boldsymbol{a}}_{\boldsymbol{iH}} \tag{10}$$

and the horizontal and vertical transmission coefficients as

$$T_H = \frac{2p_1}{p_1 + p_2}, \quad T_V = \frac{2p_1\sqrt{\epsilon}}{\epsilon p_1 + p_2}. \tag{11}$$

The transmission properties of the surface for this incident field are given by the transmission dyadic

$$\overline{\boldsymbol{T}} = \begin{cases} \hat{\boldsymbol{a}}_{\boldsymbol{iH}} T_H \hat{\boldsymbol{a}}_{\boldsymbol{iH}} + \hat{\boldsymbol{a}}_{\boldsymbol{tV}} T_V \hat{\boldsymbol{a}}_{\boldsymbol{iV}}, & \text{if } (\hat{\boldsymbol{n}} \cdot \hat{\boldsymbol{k}}_{\boldsymbol{i}})^2 + \epsilon - 1 > 0 \\ 0, & \text{if } (\hat{\boldsymbol{n}} \cdot \hat{\boldsymbol{k}}_{\boldsymbol{i}})^2 + \epsilon - 1 \leq 0. \end{cases} \tag{12}$$

Thus, the transmitted electric field at a distance of R from $\boldsymbol{r_0}$ along the transmitted ray through $\boldsymbol{r_0}$ is

$$\boldsymbol{E_t}(\boldsymbol{r_0} + R\hat{\boldsymbol{k}}_{\boldsymbol{t}}) = \overline{\boldsymbol{T}} \cdot \boldsymbol{E}(\boldsymbol{r_0}) e^{ikR\sqrt{\epsilon}} \sqrt{\frac{\rho_1' \rho_2'}{(\rho_1' + R)(\rho_2' + R)}} \tag{13}$$

where the principal radii of curvature of the transmitted field ρ_1' and ρ_2', are the two roots of the quadratic equation in ρ'

$$\begin{aligned} (\hat{\boldsymbol{n}} \cdot \hat{\boldsymbol{k}}_{\boldsymbol{i}})^2 \rho'^2 - \rho' \sqrt{\epsilon} \Big\{ & (\rho_1 + \rho_2)(\hat{\boldsymbol{n}} \cdot \hat{\boldsymbol{k}}_{\boldsymbol{i}})^2 \\ & + \left[\rho_1 (\hat{\boldsymbol{x}}_{\boldsymbol{1}} \cdot \hat{\boldsymbol{n}})^2 + \rho_2 (\hat{\boldsymbol{x}}_{\boldsymbol{2}} \cdot \hat{\boldsymbol{n}})^2 \right] \left(1 - \frac{1}{\epsilon} \right) \Big\} \\ & + \rho_1 \rho_2 \left[\left(\hat{\boldsymbol{n}} \cdot \hat{\boldsymbol{k}}_{\boldsymbol{i}} \right)^2 + \epsilon - 1 \right] = 0. \end{aligned} \tag{14}$$

If the point of incidence $\boldsymbol{r_0}$ lies on an edge of the scattering object then the incident ray will produce edge diffraction rays. The direction of the diffracted ray will be denoted $\hat{\boldsymbol{k}}_{\boldsymbol{s}}$ and the distance along this ray from the point of diffraction at $\boldsymbol{r_0}$ will be denoted R_s. We define k_s as the wavenumber of the medium in which the diffracted ray propagates

$$k_s = \begin{cases} k, & \text{if } \hat{\boldsymbol{k}}_{\boldsymbol{s}} \text{ is exterior} \\ k\sqrt{\epsilon}, & \text{if } \hat{\boldsymbol{k}}_{\boldsymbol{s}} \text{ is interior.} \end{cases} \tag{15}$$

Then we introduce the modifications in [5] to

$$\boldsymbol{b} = \frac{k}{k_s} \hat{\boldsymbol{k}}_{\boldsymbol{i}} - \hat{\boldsymbol{k}}_{\boldsymbol{s}} \tag{16}$$

$$\overline{\boldsymbol{C}} = \frac{\overline{\boldsymbol{I}} - \hat{\boldsymbol{k}}_{\boldsymbol{s}} \hat{\boldsymbol{k}}_{\boldsymbol{s}}}{R_s} + \frac{k}{k_s} \left[\frac{\hat{\boldsymbol{x}}_{\boldsymbol{1}} \hat{\boldsymbol{x}}_{\boldsymbol{1}}}{\rho_1} + \frac{\hat{\boldsymbol{x}}_{\boldsymbol{2}} \hat{\boldsymbol{x}}_{\boldsymbol{2}}}{\rho_2} \right]. \tag{17}$$

Then

$$\overline{\boldsymbol{M}} = \begin{cases} \left(\overline{\boldsymbol{I}} - \hat{\boldsymbol{k}}_{\boldsymbol{s}} \hat{\boldsymbol{k}}_{\boldsymbol{s}} \right) \cdot \Big[\left(\overline{\boldsymbol{I}} + \overline{\boldsymbol{R}} \right) \left(\hat{\boldsymbol{n}} \cdot \hat{\boldsymbol{k}}_{\boldsymbol{s}} \right) \\ \quad + \left(\overline{\boldsymbol{I}} - \overline{\boldsymbol{R}} \right) \left(\hat{\boldsymbol{n}} \cdot \hat{\boldsymbol{k}}_{\boldsymbol{i}} \right) \Big], & \text{if } \hat{\boldsymbol{k}}_{\boldsymbol{s}} \text{ exterior} \\ -\left(\overline{\boldsymbol{I}} - \hat{\boldsymbol{k}}_{\boldsymbol{s}} \hat{\boldsymbol{k}}_{\boldsymbol{s}} \right) \cdot \overline{\boldsymbol{T}} \hat{\boldsymbol{n}} \cdot (\hat{\boldsymbol{k}}_{\boldsymbol{s}} + \hat{\boldsymbol{k}}_{\boldsymbol{t}}), & \text{if } \hat{\boldsymbol{k}}_{\boldsymbol{s}} \text{ interior.} \end{cases} \tag{18}$$

In these expressions, $\overline{\boldsymbol{I}}$ is the unit dyadic and the vectors $\hat{\boldsymbol{e}}_{\boldsymbol{j}}$ and $\hat{\boldsymbol{i}}_{\boldsymbol{j}}$ are the usual orthonormal vectors that define the jth edge. The vector $\hat{\boldsymbol{e}}_{\boldsymbol{j}}$ is parallel to the jth edge. The vector $\hat{\boldsymbol{i}}_{\boldsymbol{j}}$ is perpendicular to $\hat{\boldsymbol{e}}_{\boldsymbol{j}}$ and the surface normal $\hat{\boldsymbol{n}}$ and points to the side of the edge on which the surface lies.

The edge-diffracted ray is limited to those directions $\hat{\boldsymbol{k}}_{\boldsymbol{s}}$ that satisfy

$$\hat{\boldsymbol{k}}_{\boldsymbol{s}} \cdot \hat{\boldsymbol{e}}_{\boldsymbol{j}} = \frac{k}{k_s} \hat{\boldsymbol{k}}_{\boldsymbol{i}} \cdot \hat{\boldsymbol{e}}_{\boldsymbol{j}}. \tag{19}$$

For exterior diffracted rays, this expression gives the familiar Keller cone of diffracted rays formed by rotating the incident ray about the edge. For interior diffracted rays this expression gives a different cone of diffracted rays formed by rotating the transmitted ray $\hat{\boldsymbol{k}}_{\boldsymbol{t}}$ about the edge.

The curvature of the field in the plane of the wedge is given by

$$\frac{1}{\rho} = \frac{k_s k}{k_s^2 - k^2 \left(\hat{\boldsymbol{k}}_{\boldsymbol{i}} \cdot \hat{\boldsymbol{e}}_{\boldsymbol{j}} \right)^2} \left[\frac{(\hat{\boldsymbol{x}}_{\boldsymbol{1}} \cdot \hat{\boldsymbol{e}}_{\boldsymbol{j}})^2}{\rho_1} + \frac{(\hat{\boldsymbol{x}}_{\boldsymbol{2}} \cdot \hat{\boldsymbol{e}}_{\boldsymbol{j}})^2}{\rho_2} \right] \tag{20}$$

and the edge-diffracted field can be written

$$\boldsymbol{E_{ej}}\left(\boldsymbol{r_0} + R_s \hat{\boldsymbol{k}}_{\boldsymbol{s}}\right) = \overline{\boldsymbol{D}}_{\boldsymbol{ej}} \cdot \boldsymbol{E_i}(\boldsymbol{r_0}) e^{ik_s R_s} \sqrt{\frac{\rho}{R_s(R_s + \rho)}}. \tag{21}$$

The edge-diffraction coefficient is

$$\overline{\boldsymbol{D}}_{\boldsymbol{ej}} = -\frac{1}{2}\,\mathrm{sign}[\hat{\boldsymbol{i}}_{\boldsymbol{j}}\cdot\boldsymbol{b}]K\left(\sqrt{\frac{k_s c_j(\hat{\boldsymbol{i}}_{\boldsymbol{j}}\cdot\boldsymbol{b})^2}{2}}\right) \cdot\sqrt{\frac{c_j k_s^2}{k_s^2 - k^2(\hat{\boldsymbol{k}}_{\boldsymbol{i}}\cdot\hat{\boldsymbol{e}}_{\boldsymbol{j}})^2}}\,\overline{\boldsymbol{M}} \tag{22}$$

where $K(\tau)$ is the modified Fresnel integral

$$K(\tau) = \frac{1}{\sqrt{\pi}}\,e^{-i[\tau^2+(\pi/4)]}\int_{\tau}^{\infty} e^{it^2}\,dt. \tag{23}$$

This more general version of POGTD compared with [5] is valid in both the exterior and interior regions; the major difference between the regions is the different expressions for $\overline{\boldsymbol{M}}$ given in (18).

To calculate the diffraction field from the wedge the edge diffraction coefficient is used each time a field is incident on the edge of a surface. The first diffracted field can be calculated by a straightforward application of (22), but the inside of the wedge must be regarded as the "exterior" region and the outside medium as the "interior" to calculate the second field.

In respect to the diffraction coefficient (22), the sign function is important as it means that each of the edge-diffracted fields, whether concerned with diffraction outside or inside the material, has two discontinuities, one at a shadow boundary and one at a reflection boundary, which compensate for the corresponding discontinuities in the geometrical optics fields. We will deal separately with plane polarized incident radiation with electric field perpendicular to the plane of incidence (horizontal polarization, TE, "hard" polarization) and parallel to the plane of incidence (vertical polarization, TM, "soft" polarization). The separation between the source and wedge is assumed to be large enough to use plane wave reflection and transmission coefficients given by the Fresnel equations. Transmission of the incident radiation through the wedge and then out again into the outside medium depends on the angle of incidence at the dense-rare interface in relation to the critical angle. We consider waves incident at the top wedge surface which are reflected at the surface and diffracted on the outside at the edge of the wedge, waves that are transmitted into the medium through the top surface and diffracted at the edge of the wedge from inside, and finally, the waves transmitted at the bottom surface or internally reflected by it.

III. Experimental

Dielectric wedges were fabricated in a light gypsum cement ($\epsilon = 3.1$ for 1 cm wavelength microwaves) and a polymer mixture in styrene, "resin C" ($\epsilon = 1.86$), supplied by Scott Bader, Ltd. Typical wedge dimensions for both materials were ~70 cm hypotenuse, made to define wedge angles at the apex of a triangle of 20°, 30°, 60°, 90°; the wedge depth was ~30 cm. The mass of each wedge was about 35 kg. Both types of wedge had to be made in layers of material to ensure even drying and/or to allow heat to dissipate; the layering, particularly for the gypsum wedge, gave rise to some sharp small-angle scattering superimposed on the shadow region. The experimental arrangement for the incidence of microwaves on a wedge was as in Fig. 1. Effects due to the finite wedge dimensions were small, but some improvement in signal to noise ratio was achieved by placing radar absorbing sheet along the sides and the base of the wedge. The surfaces of the wedges were macroscopically smooth and the effects of scattering from the surface roughness for waves of 1-cm wavelength is negligible.

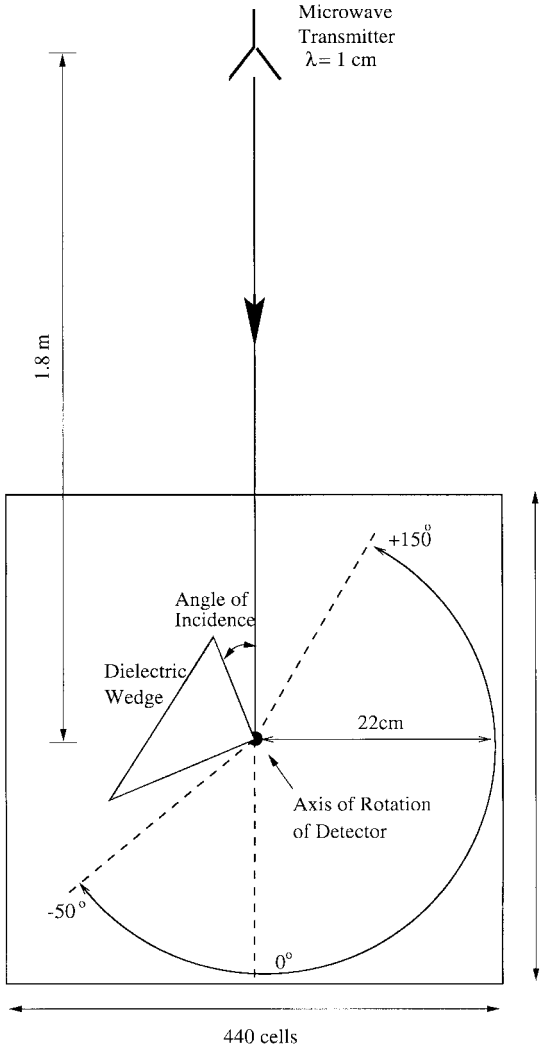

Fig. 1. Schematic diagram of experimental determination of scattering from dielectric wedge. Also shown is the disposition of the cells (pixels) used in the FDTD calculations of the scattered field.

Both TE and TM linear polarizations of the incident field were used with the electric vector either parallel or perpendicular to the edge, respectively, and the copolar components were measured of the scattered field. The circuitry for the measurements was generally as in [6]. A modulator is used to power a 30-GHz Gunn diode source (~110 mW) and to provide a reference signal for the lock-in amplifier. The source feeds a transmit chain, which includes an isolator to prevent backward reflected waves reaching the source, a precision calibrated attenuator, and a pyramidal horn antenna as transmitter. The source was an approximately spherically diverging, linearly polarized electromagnetic field at the apex of the dielectric wedge with an amplitude taper. The calibrated detector utilized a modified open-ended waveguide with diode

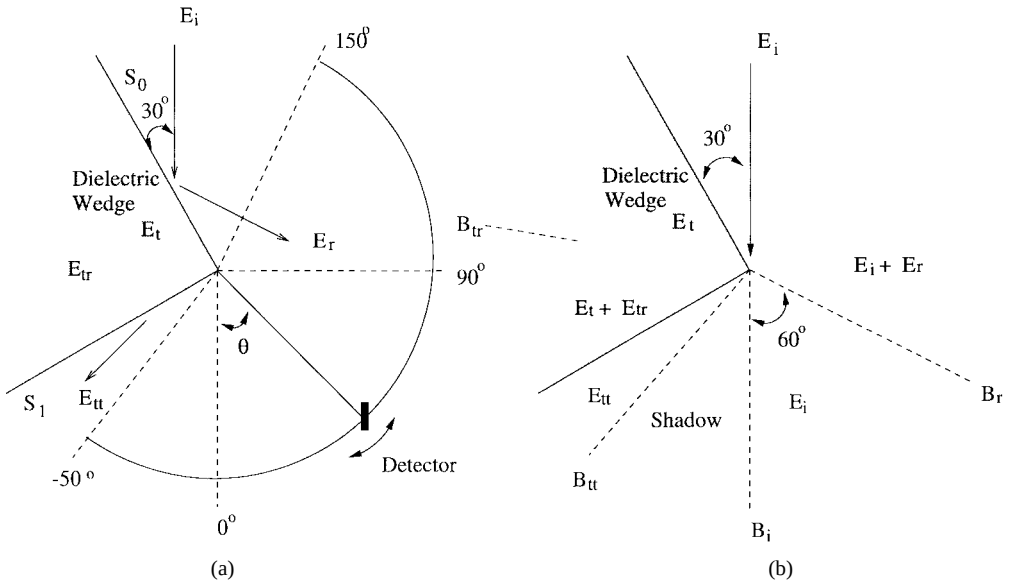

Fig. 2. (a) General indication of incident and scattered fields by dielectric wedge and angular range of measurement. (b) Regions where the various field components exist, excluding the diffraction terms at the shadow (for finite transmission) and reflection boundaries.

detector as a small area field probe with a lock-in amplifier to discriminate against noise. The wedge was mounted on a motor driven turntable with one-half degree steps with the apex of the wedge aligned as closely as possible with the rotation axis of the turntable. The effects of random and systematic errors on the measurement of scattered intensity were assessed as 2–3% from repeat runs with independent settings of the wedge relative to the rotation axis.

The detector aperture was 0.7 cm (horizontal) $\times$ 0.35 cm with a horizontal resolution of 1.8°. Calibration measurements of scattered intensity were carried out with transmitting wedges and an increased detector to wedge apex distance of 50 cm to check for possible limitations on the measured data due to detector aperture convolution. Any convolution effects were negligible and the smaller radius was preferred to increase data throughput. Using laser fiducials, much effort was expended in aligning the targets relative to the incident beam. The separation was 1.8 m between the source and the apex of the scattering wedge. Measurements to assess the diffraction coefficient were taken for detector angles from $+150°$ to $-50°$ with respect to the coordinate system defined in Fig. 1 and for both TE and TM polarizations. A large data base has been acquired of scattering results for the two polarizations, and various angles of incidence. The size of the anechoic chamber was limited by the space available to dimensions 3 m $\times$ 3 m $\times$ 4 m and the scattering measurements are in near field.

IV. Qualitative Interpretation of Experimental Data

To illustrate the intensity distribution of diffracted and scattered radiation, we consider the right-angled dielectric wedge illustrated in Fig. 2(a) and (b) and a plane wave incident at 30° to the surface S_0 of the wedge and in the plane perpendicular to the edge of the wedge. The angular incidence is defined relative to the surface to give a continuous angular range from 10 to 130°. Fig. 2(a) shows the general disposition of the electromagnetic fields and Fig. 2(b) shows the regions where the fields exist and the field boundaries. Additional reflected and/or transmitted rays may arise by multiple reflection inside the wedge and emerge if incident at the interface at angles less than the critical angle; such rays, for the wedges used, exist in directions close to the wedge surfaces and are outside the angular range of the experimental measurements.

For dielectrics in the experimental angular range, excluding multiple interactions, the geometrical optics field consists of up to 5 fields, the incident field $\boldsymbol{E_i}$, the reflected and transmitted fields, $\boldsymbol{E_r}$ and $\boldsymbol{E_t}$, by surface S_0, and the fields that are reflected and transmitted, $\boldsymbol{E_{tr}}$ and $\boldsymbol{E_{tt}}$, when the field meets the second surface S_1. In addition to the interactions of the geometrical optics field, there are also fields due to diffraction at the edge of the wedge for both external and internal interactions.

The boundaries B_i and B_r (for a given angle of incidence) are fixed and, in the given example, for 30° incidence their angular locations are defined as 0° and $+60°$, respectively; that is, the boundary B_i is taken as the origin of the angular position of the detector. The angular position of B_r relative to this origin is twice the wedge angle. The positions of the boundaries B_{tr} and B_{tt} depend on the refractive index of the wedge (through the critical angle). As the refractive index of the wedge increases, both B_{tr} and B_{tt} rotate about the edge toward the surface S_1. The boundary B_{tr} only reaches the surface in the limit of infinite refractive index, but the boundary B_{tt} reaches the surface S_1 when the field $\boldsymbol{E_t}$ strikes S_1 at the critical angle. Beyond this point the field $\boldsymbol{E_t}$ is totally internally reflected at this surface and the field $\boldsymbol{E_{tt}}$ and its boundary B_{tt} cease to exist.

Concerning the distribution of scattered intensity, in the region of overlap of the waves $\boldsymbol{E_i}$ and $\boldsymbol{E_r}$, interference fringes are expected parallel to the edge of the wedge: there is also a small effect due to interference with externally diffracted rays

TABLE I
EXPERIMENTAL ROTATIONAL AND DISPLACEMENT ERRORS IN 90° WEDGE SETTING

Angle of Incidence (to surface)	TE Measurements		TM Measurements	
	Rotation	Displacement	Rotation	Displacement
40°	2.0°	1.8cm	0.0°	1.8cm
30°	3.0°	2.2cm	1.0°	2.2cm
20°	1.3°	1.3cm	1.0°	3.5cm

for angles greater than that corresponding to B_r. Between B_r and B_i the only geometrical optics field is the incident $\boldsymbol{E_i}$ and on this basis the field would be constant, but in practice here we have the overlap and interference of $\boldsymbol{E_i}$ with the external wedge diffraction. From B_i to B_{tt} the geometrical shadow is found. Because of diffraction, there is a profile of intensity on each of the demarcations of the geometrical shadow due on the reflection side of the shadow region to wedge diffraction at the outside of the edge and on the transmission side of the shadow boundary, for incidence at face S_1, at angles less than the critical angle, to diffraction at the edge in transmission. Concerning the diffracted fields from the edge of the wedge, these two fields are expected to show maxima at the boundaries of the geometrical optics field, i.e., for diffraction at the outside edge we expect maxima at +60° (B_r, reflection boundary) and 0°. For diffraction at the edge from inside we expect maxima of the diffraction coefficient at B_{tt} and B_{tr}.

The distribution of scattered intensity and the angular range of measurement is markedly dependent on the beam profile incident from the antenna. The experimental angular profiles, with full width at half maximum (FWHM) of ∼60°, of the microwave intensity incident on the wedges are shown in Fig. 3 for both TE and TM polarizations: the differences in beam shape of the polarized beams are small. Also shown is a Gaussian fit to the intensity profiles, considered to be adequate for both polarizations, which was used to describe the input field in the calculations by POGTD and in the calculations carried out using FDTD.

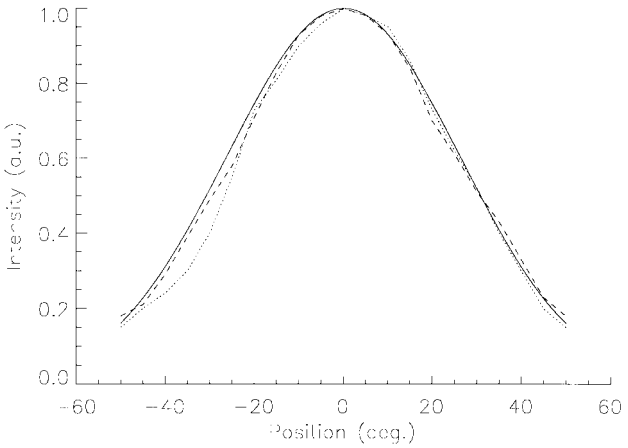

Fig. 3. Measured incident microwave beam profiles for TE (dotted line) and TM (dashed line) polarization and fitted Gaussian profile (full line).

V. CALIBRATION OF EXPERIMENTAL DATA: FDTD CALCULATIONS

The scattering data were affected by small misplacements of the apex and misalignments of the edge of the wedge relative to the center of the broad incident microwave beam. To assess these errors and to gain an independent set of calculated scattered intensities to compare with the experimental data, representative calculations for dielectric wedges were undertaken using the Mission Research Corporation's "MAGIC" FDTD software package. The available package of 200 000 cells (pixels) provided a solution to the full-vector Maxwell equations in two dimensions.

For good convergence of the MAGIC program, fields were spatially sampled at one tenth wavelength intervals, i.e., at 1-mm intervals in the setup of Fig. 1. This figure shows the sampling scheme adopted by which $440 \times 440 = 193\,600$ cells were distributed over the scatterer and the region of detection. The Gaussian source distribution (Fig. 3) was used to specify the input field. To prevent extraneous reflections from the mesh boundaries, the area of computation was enclosed in barriers with strong absorption. To produce a time-averaged field intensity, calculations of the full 2-D electric field distribution were made at either ∼1/2 or ∼1 p/s intervals throughout the 33.3 p/s periodicity of the incident microwaves and the results summed and averaged. Errors in the position of the edge of the wedge and of the axis of rotation relative to the wedge apex were corrected by bringing the angular positions of the peaks in the experimental results into agreement with the peaks of the FDTD distributions. Examples, for TE and TM polarization, of the rotational and displacement errors for 20°, 30°, and 40° angles of incidence on the 90° wedge with $\epsilon = 3.1$ are given in Table I. The range of values of wedge rotation and displacement errors, with a different set for each wedge placement and polarization change, is representative of the experimental problems, particularly to define the axis of the broad microwave beam.

VI. CALCULATION OF SCATTERED INTENSITY FROM DIELECTRIC WEDGES BY POGTD

Illustrative cases of the dissection for POGTD (separately for TE and TM) of the scattered amplitude into components corresponding to different types of interaction, namely the total geometrical optics field and the total diffracted field and the resultant total intensity curves, are shown in Fig. 4(a)–(d) for a 60° wedge and 30° angle of incidence $\epsilon = 1.86$. The diffracted component rises to peaks at the boundaries of the geometrical optics field. The calculations assume an incident plane wave but otherwise use the dimensions of the experimental rig. Both the outside- and inside-wedge diffraction coefficients are excited. The main differences between TE and TM intensity distributions are due to the different Fresnel reflection and

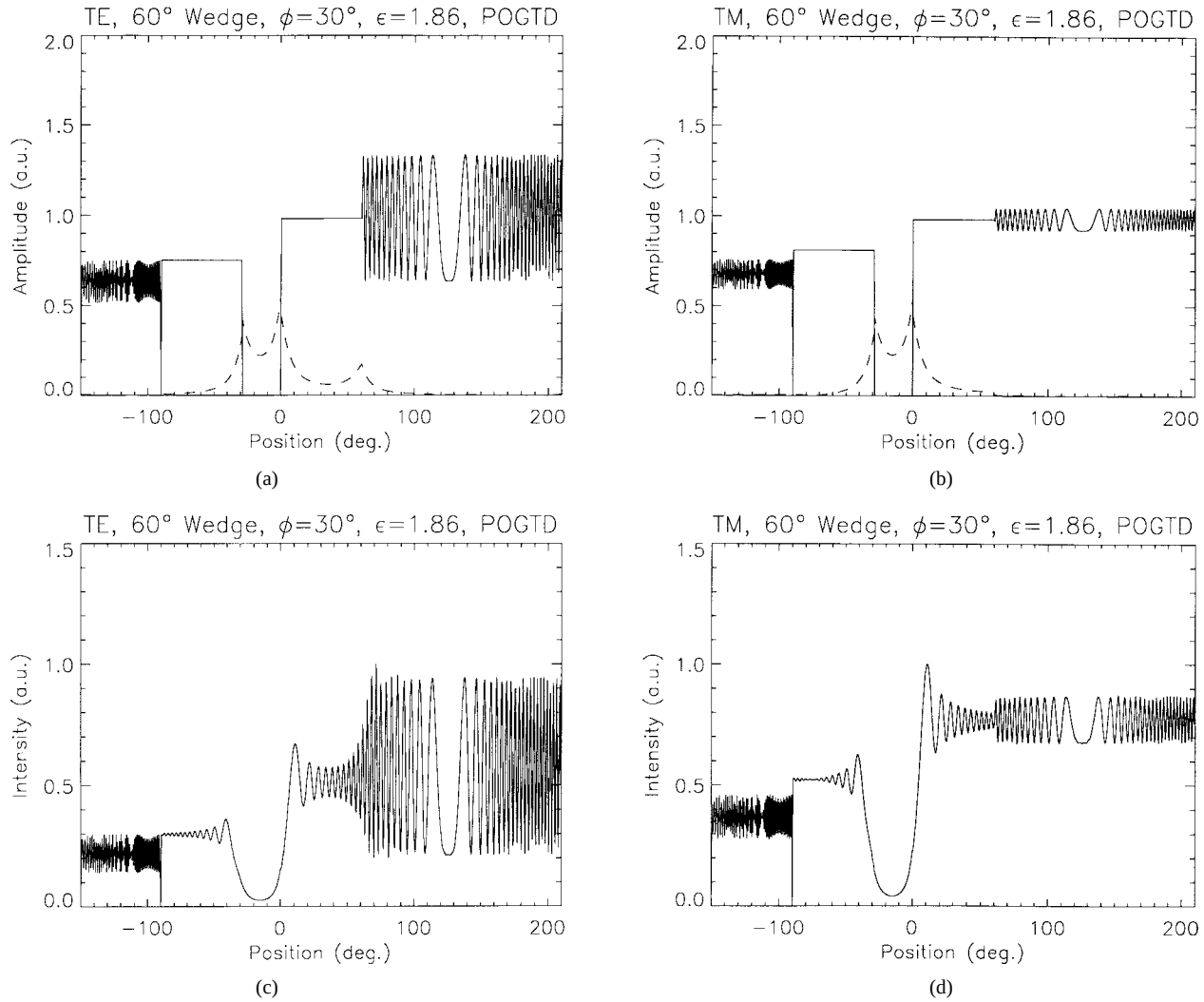

Fig. 4. (a) Separate amplitude presentations for incident plane wave $\epsilon = 1.86$ of classical geometrical edge profile and edge diffraction for TE polarization, 60° wedge angle, 30° angle of incidence. (b) Total intensity distribution corresponding to (a). (c) As 4(a) for TM polarization. (d) Total intensity distribution corresponding to (c). Dotted curves in (a) and (b) correspond to total diffracted fields.

transmission coefficients. The curves in Fig. 5(a)–(d), again for TE and TM polarization, respectively, show the same separate components of the scattered amplitude and the total intensity but for the incidence of a microwave beam with the broad Gaussian shape corresponding to the experimental source of Fig. 3. There is a marked change in the shape of the intensity distribution which now takes the form of a peak centered about boundary B_i with fluctuations and decreasing rapidly in intensity with increasing angles on either side.

VII. Experimental Scattering by Dielectric Wedges: Comparisons with POGTD and FDTD

The complete set of experimental results covers wedge angles of 20° (only for $\epsilon = 3.1$), 30°, 60°, and 90° for TE and TM polarization, dielectric wedges with $\epsilon = 1.86$, 3.1, angles of incidence from 10° up to in some cases 130°, plus corresponding POGTD calculations from 10° incidence in steps of 10°. Besides the FDTD calculations referred to above, calculations were undertaken for $\epsilon = 3.1$, the 30° wedge and angles of incidence of 30°, 60°, 80°, 90°, and 100°. A selection of these results is considered below.

All three sets of results, experimental, POGTD, and FDTD are independently normalized to the incident intensity and a valid comparison of intensity levels can be made. Experimental and POGTD results are compared in Fig. 6 (30° wedge, $\epsilon = 1.86$, angle of incidence ϕ from 20° to 90° as marked) and Fig. 7 (60° wedge, $\epsilon = 1.86$, ϕ from 20° to 70°). The left-hand column in each figure gives TE data and the right column gives TM data. Experimental results for 60° and 90° wedges, were taken for TE only, respectively, with permittivities of 3.1 and 1.86, angle of incidence from 20° to 70°. The angular range of experimental measurement is reduced in some results as the detector intersected the side of the wedge and/or there was no transmission when the critical angle was exceeded at the emergent interface. For the 60° wedge and the higher ϵ and for all angles of incidence, rays transmitted into the wedge are totally internally reflected at the second surface and only one side of the shadow region is observed. For the 90° wedge of either ϵ and for all angles of incidence, there are no transmitted rays.

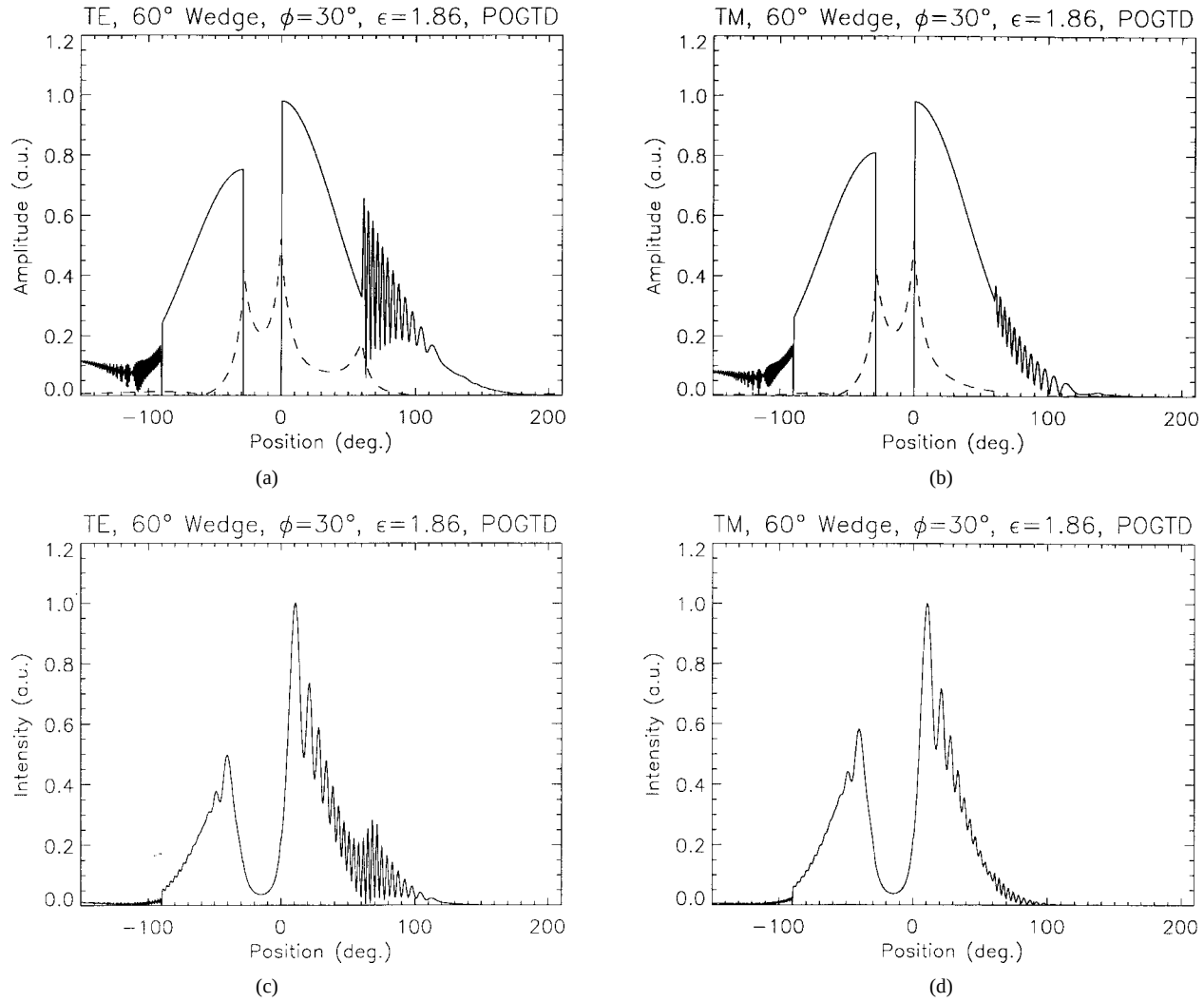

Fig. 5. (a)–(d): As Figs. 4(a)–(d) but for incident microwave beam with Gaussian profile; profile as in Fig. 3. Dotted curves in (a) and (b) correspond to total diffracted fields.

Considering the experimental results, for all angles of incidence and all wedge angles on wedges of the same material, the intensity distributions are effectively identical for all angles from B_i, the position of the intensity peak near the reflection-side shadow boundary extending toward B_r (i.e., when the overlapping features arising by interference of $\boldsymbol{E_r}$ have been moved to higher angles revealing the interference between the direct beam and the external diffraction). For wedges of different wedge angle at all angles of incidence and with the two values of permittivity the differences in the intensity distributions in this angular range are small. In experimental terms, there is effectively an intensity distribution of closely constant shape, which defines, in the angular region from B_i to B_r, the interference between the incident beam and the external diffracted rays at the dielectric wedge. The comparisons in the figures between the experimental data and POGTD in this angular range, including the interference at higher angles between the incident and directly reflected rays, show good agreement and a weak dependence of the external diffraction coefficient on permittivity.

Considering the overall results of Figs. 6 and 7, POGTD provides a reasonable smooth fit to the intensity levels of the experimental data over the whole of the patterns for angles of incidence from small values up to near normal incidence for both TE and TM. For angles of incidence greater than normal the POGTD results, calculated without account of absorption beyond the shadow boundary B_{tt}, particularly for TE for the higher permittivity and TM at the lower permittivity, for angles between B_{tt} and the side of the wedge, tend to be too high. When the diffraction about B_{tt} is excited at a given angle of incidence; then, for that wedge angle, the peak intensity at the transmission side of the shadow region increases with increasing angle of incidence consistent with increasing transmitted intensity. The peak transmitted intensity for the wedge with lower permittivity is much greater than that for the gypsum wedge with the same wedge angle and angle of incidence and occurs at a smaller angle of deviation.

Fig. 8 shows a comparison for TE and TM polarizations between the experimental, POGTD, and FDTD sets of data for the 30° wedge, $\epsilon = 3.1$ for a range of angles of incidence. Only the diffraction on the reflection side of the shadow region is found for incident angles of 100° and larger. The absorption parameter for the FDTD calculations was set by fitting the experimental and calculated curves at 30° incident

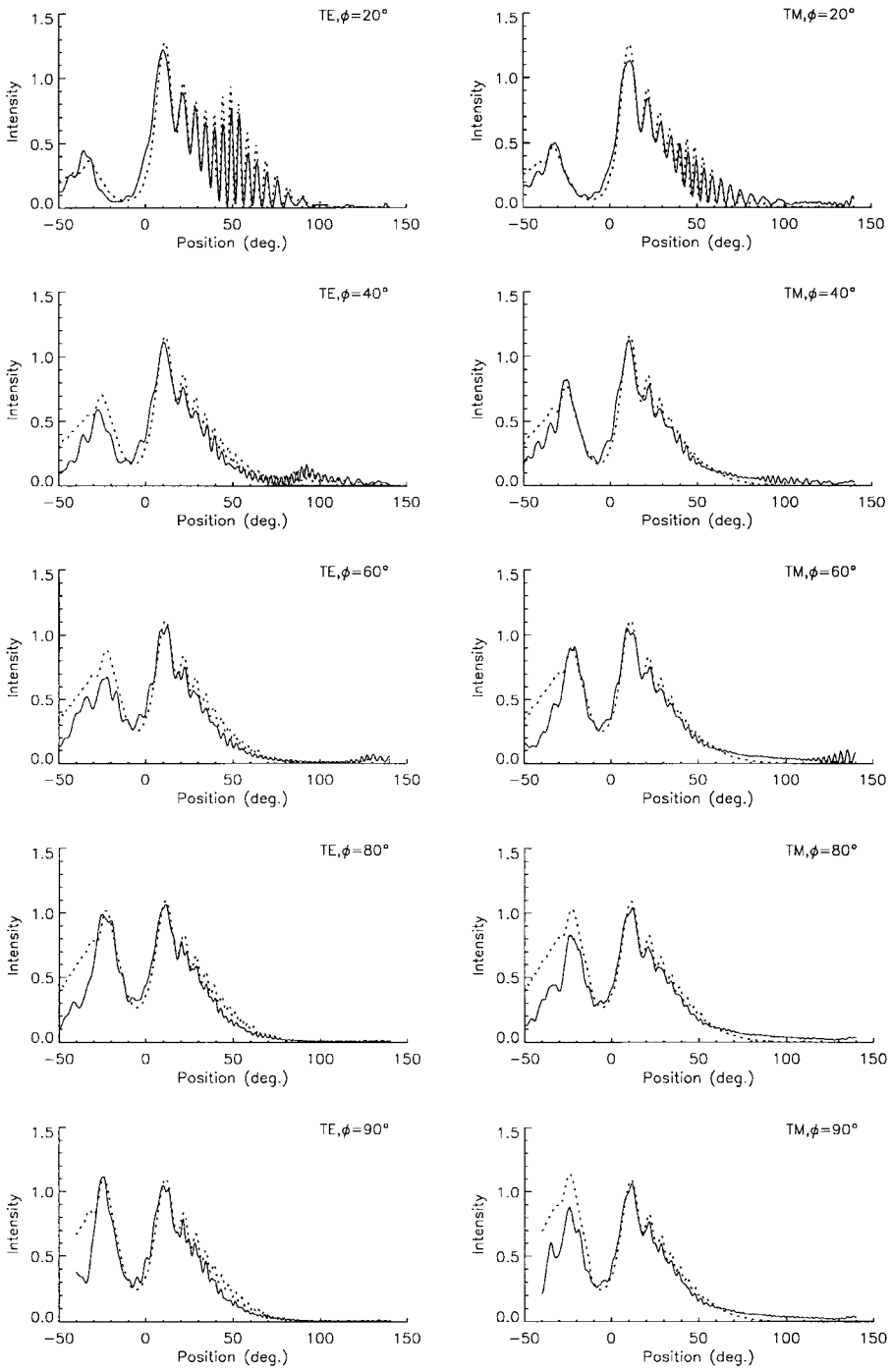

Fig. 6. Experimental (full line) and POGTD (dotted line) intensity distributions for 30° wedge and $\epsilon = 1.86$. Left side—TE; right side—TM. Angles of incidence to wedge surface as marked range from 20° to 90°.

angle; the corresponding loss tangent was 3×10^{-2}, somewhat higher than the experimental value. The agreement between all three curves is excellent on the reflection side of the shadow region in intensity level and the features of the intensity distributions. In the shadow region the experimental results are affected by small diffraction peaks attributed to the layering due to the method of fabricating the gypsum wedges. In the shadow region, the FDTD results show a definite fringing structure of low intensity superimposed on the intensity minimum defining the shadow region that is especially prominent for 60° angle of incidence decreasing in intensity for other incident angles greater and smaller. Comparing the experimental results as a whole (Figs. 5–7 and results not published) with the FDTD results (in the absence of particle size effects), small fluctuations in the intensity distribution within the shadow region are evident, prominent for the smaller angles of incidence as found in the FDTD calculations. The POGTD calculations for the transmission boundary of the shadow region are of the correct general shape but overestimate the transmitted intensity by an increasing

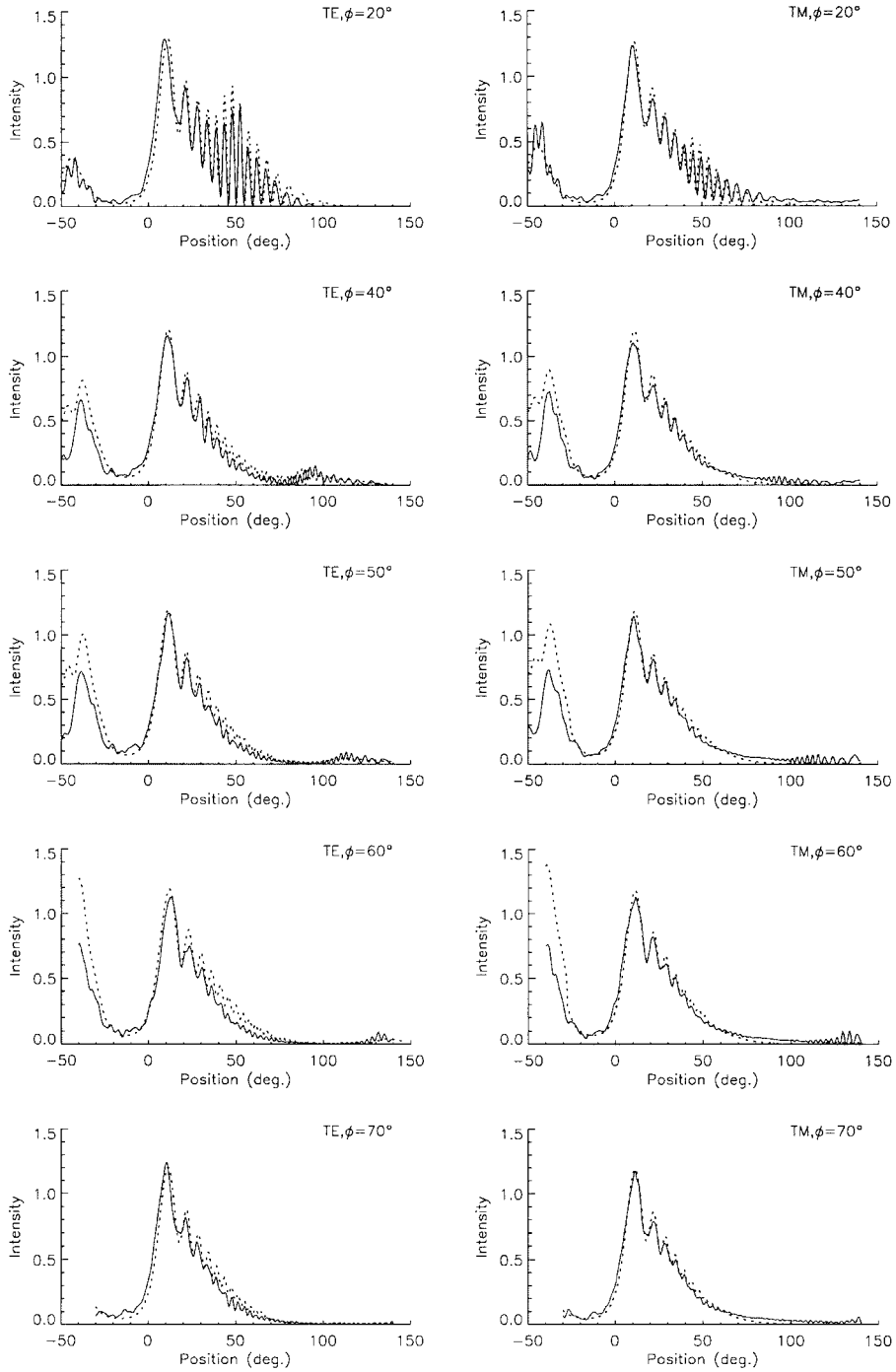

Fig. 7. Experimental (full line) and POGTD (dotted line) intensity distributions for 60° wedge and $\epsilon = 1.86$. Left side—TE; right side—TM. Angles of incidence to wedge surface as marked range from 20° to 70°.

amount with a maximum ratio of about 1.5, as the angle of incidence increases beyond normal. This is due to the neglect of absorption. The POGTD results do not show the superimposed small intensity peaks in the shadow region.

VIII. Conclusion

Total agreement between the experimental and FDTD calculated results cannot be expected in practice, even if expected in principle for a fully specified object model, if the calculations were free of all sampling errors, because the experimental wedges are not of homogeneous composition and are not necessarily free of small voids, the edges of the wedges have finite thickness, etc. Nevertheless, the agreement between the experimental results and the FDTD results overall accounting for absorption, is very satisfactory.

The agreement between the experimental scattered intensity and the results of both calculations show that the diffraction coefficient derived from POGTD is entirely satisfactory for diffraction on the reflection side of the shadow boundary of the dielectric wedge; this shows a weak dependence on dielectric permittivity. The most serious difference between

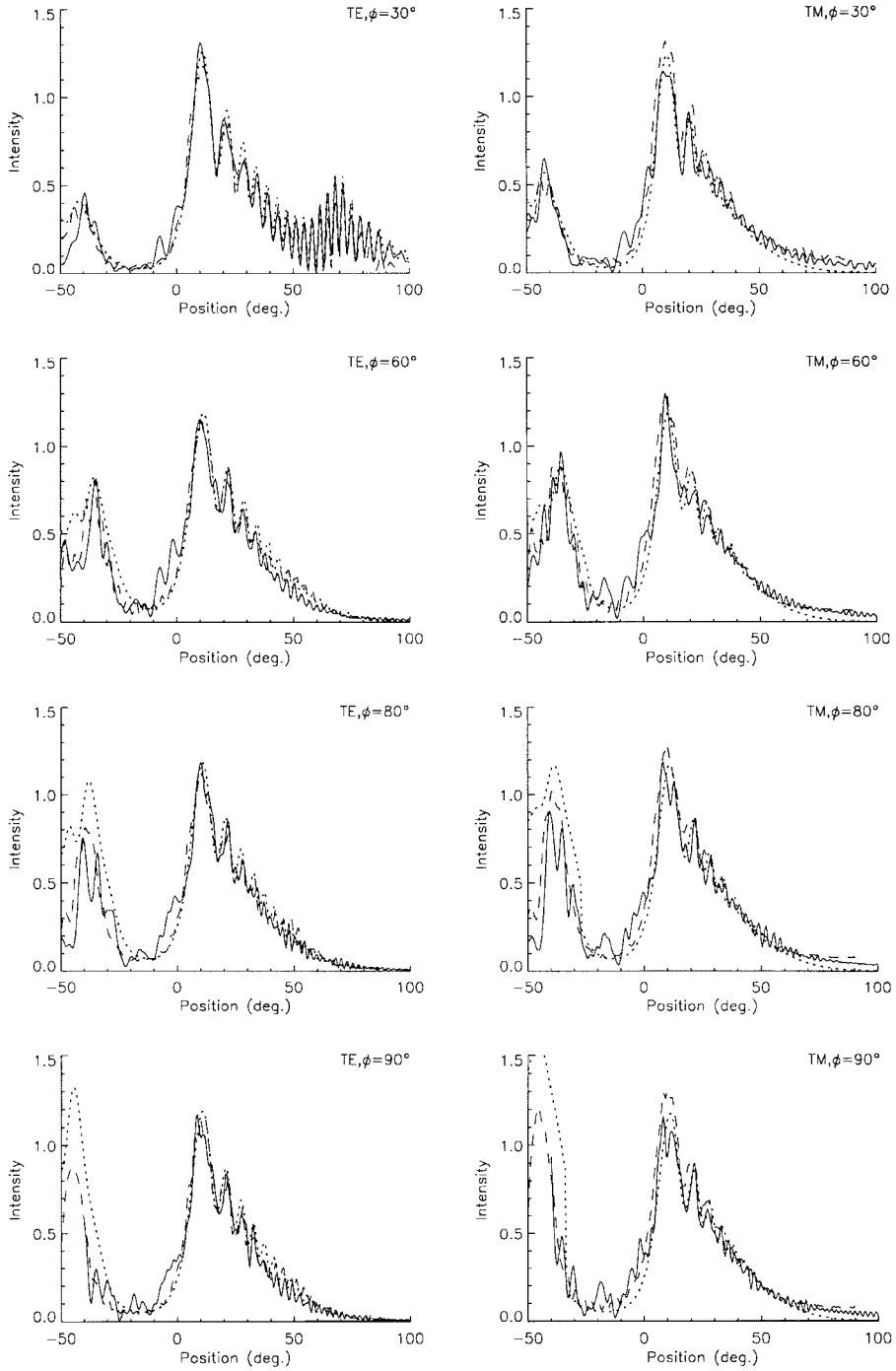

Fig. 8. Experimental (full line), FDTD (dashed line) and POGTD (dotted line) intensity distributions for 30° wedge and $\epsilon = 3.1$. Left side—TE; right side—TM. Angles of incidence to wedge surface 30°, 60°, 80°, and 90°.

the experimental and POGTD results is in the magnitude of the diffraction coefficient, following the assumption of zero absorption, at the transmission side of the shadow boundary and for angles of incidence greater than normal. Absorption can readily be introduced empirically into POGTD, necessarily based on an assumption of the dielectric permittivity of the material, according to a judgement of the angle of incidence at a dielectric edge. The comparison between POGTD and FDTD calculations, in respect of the small intensity fluctuations in the shadow region, reveals effects that probably concern surface waves excited on one or both of the wedge surfaces, according to whether external or internal diffraction is excited or both and strongly excited in a particular angular range [24], [26], [30] away from normal incidence. Of course, the SAR simulator applies to far-field rather than the near-field conditions of these experiments; the formulation of the diffraction coefficient for the dielectric edge accommodates this.

ACKNOWLEDGMENT

The authors would like to thank Dr. D. Blacknell of DERA, Malvern, for his discussion. They would also like to thank

Mission Research Corporation, Newington, VA, and particularly L. Ludeking, for making the "MAGIC" FDTD software available. R. E. Burge would like to thank Profs. A. Howie and M. Brown for use of the facilities in Cambridge.

REFERENCES

[1] N. T. Taket, S. M. Howarth, and R. E. Burge, "A model for the imaging of urban areas by synthetic aperture radar," *IEEE Trans. Geosci. Remote Sensing*, vol. 29, pp. 432–443, May 1991.
[2] E. F. Knott, J. F. Shaeffer, and M. T. Tuley, *Radar Cross Section.* Norwood, MA: Artech House, 1985.
[3] A. van der Merwe, M. J. Gerry, L. C. Potter, and I. J. Gupta, "Feature estimation using a two-dimensional parametric model of radar scattering," in *Proc. SPIE, Algorithms for Synthetic Aperture Radar Imaging IV*, vol. 3070, pp. 322–333, 1997.
[4] J. B. Keller, "Diffraction by an aperture," *J. Appl. Phys.*, vol. 28, pp. 426–444, 1957.
[5] N. D. Taket and R. E. Burge, "A physical optics version of the geometrical theory of diffraction," *IEEE Trans. Antennas Propagat.*, vol. 39, pp. 719–731, June 1991.
[6] B. D. Carroll and R. E. Burge, "Experimental confirmation of recent results in GTD applied to a conducting quarter plate," *J. Mod. Opt.*, vol. 39, pp. 1205–1220, 1992.
[7] R. G. Kouyoumjian and P. H. Pathak, "A uniform geometrical theory of diffraction for an edge in a perfectly conducting surface," *Proc. IEEE*, vol. 62, pp. 1448–1461, Nov. 1974.
[8] S. W. Lee and G. A. Deschamps, "A uniform asymptotic theory of electromagnetic diffraction by a curved wedge," *IEEE Trans. Antennas Propagat.*, vol. 24, pp. 25–34, Jan. 1976.
[9] C. W. Chuang and M. C. Liang, "A uniform asymptotic analysis of the diffraction by an edge in a curved screen," *Radio Sci.*, vol. 23, pp. 781–790, 1988.
[10] M. C. Liang, C. W. Chuang, and P. H. Pathak, "A generalized uniform geometrical theory of diffraction ray solution for the diffraction by a wedge with convex faces," *Radio Sci.*, vol. 31, pp. 679–691, 1996.
[11] R. J. Luebbers, "Propagation prediction for hilly terrain using GTD wedge diffraction," *IEEE Trans. Antennas Propagat.*, vol. AP-32, pp. 951–955, Sept. 1984.
[12] B. J. Rubin, "General solution for propagation, radiation and scattering in arbitrary 3-D inhomogeneous structures," *IEEE Antennas Propagat. Mag.*, vol. 34, pp. 17–25, Feb. 1992.
[13] D. H. Schaubert, D. R. Wilton, and A. W. Glisson, "A tetrahedral modeling method for electromagnetic scattering by arbitrarily shaped inhomogeneous dielectric bodies," *IEEE Trans. Antennas Propagat.*, vol. AP-32, pp. 77–85, Jan. 1984.
[14] T. K. Sarkar, E. Arvas, and S. Ponnapalli, "Electromagnetic scattering from dielectric bodies," *IEEE Trans. Antennas Propagat.*, vol. 37, pp. 673–676, May 1989.
[15] B. J. Rubin and S. Daijavad, "Radiation and scattering from structures involving finite-size dielectric regions," *IEEE Trans. Antennas Propagat.*, vol. 38, pp. 1863–1873, Nov. 1990.
[16] A. W. Glisson, "An integral equation for electromagnetic scattering from homogeneous dielectric bodies," *IEEE Trans. Antennas Propagat.*, vol. AP-32, pp. 173–175, Feb. 1984.
[17] K. Umashankar, A. Taflove, and S. M. Rao, "Electromagnetic scattering by arbitrary shaped three-dimensional homogeneous lossy dielectric objects," *IEEE Trans. Antennas Propagat.*, vol. AP-34, pp. 758–766, June 1986.
[18] A. Taflove, K. R. Umashankar, and T. G. Jurgens, "Validation of FD-TD modeling of the radar cross section of three-dimensional structures spanning up to five wavelengths," *IEEE Trans. Antennas Propagat.*, vol. AP-33, pp. 662–666, June 1985.
[19] K. T. Shlager and J. B. Schneider, "A selective survey of the finite-difference time-domain literature," *IEEE Antennas Propagat. Mag.*, vol. 37, pp. 39–56, Aug. 1995.
[20] R. A. Ross, "Radar cross section of rectangular flat plates as a function of aspect angle," *IEEE Trans. Antennas Propagat.*, vol. AP-14, pp. 329–335, May 1966.
[21] T. Griesser and C. A. Balanis, "Backscatter analysis of dihedral corner reflectors using physical optics and the physical theory of diffraction," *IEEE Trans. Antennas Propagat.*, vol. AP-35, pp. 1137–1147, Oct. 1987.
[22] J. L. Volakis, W. T. Burnside, and L. Peters, "Electromagnetic scattering from appendages on a smooth surface," *IEEE Trans. Antennas Propagat.*, vol. AP-33, pp. 736–743, July 1985.
[23] R. Tiberio, G. Pelosi, and G. Manara, "A uniform GTD formulation for the diffraction by a wedge with impedance faces," *IEEE Trans. Antennas Propagat.*, vol. AP-33, pp. 867–873, Aug. 1985.
[24] T. Griesser and C. A. Balanis, "Reflections, diffractions, and surface waves for an interior impedance wedge of arbitrary angle," *IEEE Trans. Antennas Propagat.*, vol. 37, pp. 927–935, July 1989.
[25] R. Tiberio and G. Pelosi, "High-frequency scattering from the edges of impedance discontinuities on a flat plane," *IEEE Trans. Antennas Propagat.*, vol. AP-31, pp. 590–596, Apr. 1983.
[26] W. D. Burnside and K. W. Burgener, "High frequency scattering by a thin lossless dielectric slab," *IEEE Trans. Antennas Propagat.*, vol. AP-31, pp. 104–110, Jan. 1983.
[27] P. M. Morse and H. Feshbach, *Methods of Theoretical Physics.* New York: McGraw-Hill, 1953, ch. 13.
[28] N. G. Van Kampen, "An asymptotic treatment of diffraction problems," *Physica*, vol. 14, pp. 575–589, 1949.
[29] M. Idemen, "Diffraction of an obliquely incident high-frequency wave by a cylindrical curved sheet," *IEEE Trans. Antennas Propagat.*, vol. AP-34, pp. 181–187, Feb. 1986.
[30] G. D. Maliuzhinets, "Excitation, reflection and emission of surface waves from a wedge with given face impedances," *Sov. Phys. Doklady*, vol. 3, pp. 752–755, 1958.

R. E. Burge received the B.Sc., Ph.D., and D.Sc. degrees from London University, U.K., in 1953, 1957, and 1975, respectively.

He is currently a Wheatstone Professor of physics at King's College, London, U.K. He was also Director of a Leverhulme Trust Project on soft X-ray imaging at the University of Cambridge, U.K., from 1994 to 1998. His research interests involve scattering, synthetic aperture radar, image analysis, X-ray, and electron microscopy.

Dr. Burge is a fellow of the Institute of Physics and Chartered Physicist.

X.-C. Yuan received the B.Eng. and M.Eng. degrees from Tianjin University, PR, China, in 1985 and 1988, respectively, and the Ph.D. degree from London University, U.K., in 1994.

He is currently employed at Cavendish Laboratory, Cambridge University, U.K. His research interests include electromagnetic scattering, image analysis, X-ray microscopy, microstructures, and near-field optics.

B. D. Carroll received the B.Sc. degree in physics and the M.Sc. degree in applied optics, both from the Imperial College, University of London, U.K., in 1984 and 1985, respectively, and the Ph.D. degree in microwave scattering and synthetic aperture radar (SAR) from King's College, University, London, in 1990.

From 1990 and 1994, he was a Lecturer in the Department of Physics at King's College and also had research interests in experimental, computational and analytic approaches to electromagnetic scattering and imaging, particularly in application to SAR. He is currently an Engineering Consultant and Manager of the Image Processing, Mathematical Modeling, and Optical Engineering Departments at Marconi Avionics Ltd., Basildon, Essex, U.K.

N. E. Fisher received the B.Sc. and Ph.D. degrees in physics at London University, U.K.

He has since been employed as a Research Associate mainly concerned with apparatus development, computer control of equipment, and the interpretation of experimental data in solid-state and microwave physics.

T. J. Hall received the M.A. degree from Cambridge University, U.K., and the Ph.D. degree from London University, U.K., in 1977 and 1980, respectively.

He is both a Chartered Physicist and a Chartered Engineer. He began his employment as an Industrial Consultant but quickly moved to an academic career. He became a Lecturer and then a Reader of physics at King's College London, U.K., before he was appointed to his present post as Professor of Optoelectronics in the Division of Engineering, King's College, London. His research interests concern various aspects of electromagnetism including scattering, inverse problems, and image analysis, as well as device development in optoelectronics and optical processing.

G. A. Lester received the B.Sc. and Ph.D. degrees from the University of Salford, U.K., in 1985 and 1989, respectively.

He was a Research Associate in London and Manchester. He is now a Lecturer in electronics in the Department of Engineering, University of Exeter, U.K. His research interests include solutions to Maxwell equations, experimental measurements in electromagnetism, and the eletro-optic properties of liquid crystal materials and devices.

N. D. Taket received the B.A. degree in physics from Oxford University, U.K., and the Ph.D. degree from London University, U.K., in 1979 and 1983, respectively

He was with King's College, London, U.K., where his research interests included remote sensing and electromagnetic scattering from dielectric objects. He is now undertaking a career as an Actuary.

Chris J. Oliver received the B.A. degree in physics from Worcester College, Oxford, U.K., and the Ph.D. degree at Liverpool University, in 1962 and 1967, respectively.

In 1967, he joined the Photon Statistics Group at the Royal Signal and Radar Establishment (RSRE), Malvern, Australia [now the Defense Evaluation and Research Agency (DERA)]. He has led a section at the DERA (Malvern) since 1981, undertaking long-term research on the extraction and processing of information from synthetic-aperture radar (SAR) images, though recently he has become a Consultant. He was appointed Visiting Professor of physics at King's College, London, U.K., in 1987, and of Electronic Engineering at University College, London, in 1996. He is currently a Senior Research Fellow at the DERA.

Dr. Oliver was one of the joint inventors of the technique of signal-clipped photon-correlation spectroscopy exploited in the Malvern correlator, for which he won the MacRobert Award for Engineering Achievement with his coinventors in 1977.